Advances in Geo-Energy Research

Adv. Geo-energ. Res. Vol. 1, No. 3, p. 135-147, 2017
Ausasia Science and Technology Press

Original article

Numerical simulations for analyzing deformation characteristics of hydrate-bearing sediments during depressurization

Lele Liu[1,2]*, Xiaobing Lu[3], Xuhui Zhang[3], Changling Liu[1,2], Bin Du[4]

[1]*Key Laboratory of Gas Hydrate, Ministry of Land and Resources, Qingdao Institute of Marine Geology, Qingdao 266071, P. R. China.*

[2]*Evaluation and Detection Technology Laboratory of Marine Mineral Resources, Qingdao National Laboratory for Marine Science and Technology, Qingdao 266071, P. R. China.*

[3]*Institute of Mechanics, Chinese Academy of Sciences, Beijing 100190, P. R. China.*

[4]*Beijing J & C Geotechnical Construction Ltd., Beijing 100176, P. R. China.*

(Received October 8, 2017; revised October 28, 2017; accepted November 1, 2017; published December 25, 2017)

Abstract: Natural gas hydrates have been treated as a potential energy resource for decades. Understanding geomechanical properties of hydrate-bearing porous media is an essential to protect the safety of individuals and devices during hydrate production. In this work, a numerical simulator named GrapeFloater is developed to study the deformation behavior of hydrate-bearing porous media during depressurization, and the numerical simulator couples multiple processes such as conductive-convective heat transfer, two-phase fluid flow, intrinsic kinetics of hydrate dissociation, and deformation of solid skeleton. Then, a depressurization experiment is carried out to validate the numerical simulator. A parameter sensitivity analysis is performed to discuss the deformation behavior of hydrate-bearing porous media as well as its effect on production responses. Conclusions are drawn as follows: the numerical simulator named GrapeFloater predicts the experimental results well; the modulus of hydrate-bearing porous media has an obvious effect on production responses; final deformation increases with decreasing outlet pressure; both the depressurization and the modulus decrease during hydrate dissociation contribute to the deformation of hydrate-bearing porous media.

Keywords: Gas hydrate, hydrate-bearing sediment, geomechanics, depressurization, numerical simulation.

Citation: Liu, L., Lu, X., Zhang, X., et al. Numerical simulations for analyzing deformation characteristics of hydrate-bearing sediments during depressurization. *Adv. Geo-energ. Res.* 2017, 1(3): 135-147, doi: 10.26804/ager.2017.03.01.

1. Introduction

Natural gas hydrates (NGHs) are ice-like crystalline compounds formed from natural gas (methane mainly) and water at low-temperature and high-pressure conditions (Sloan and Koh, 2007). NGHs are generally found in submarine sediments along the continental margin and in permafrost regions (Boswell, 2009). One cubic metre of methane hydrate (MH) contains 0.8 m^3 of water and 164 m^3 of methane gas at standard temperature and pressure (273.15 K and 1 atm) (Boswell and Collett, 2011; Makogon et al., 2007). NGHs have drawn enormous attention throughout the world as an alternative energy resource on account of the high energy capacity, the wide distribution, and the vast reserves (Collett et al., 2015; Vedachalam et al., 2015; Chong et al., 2016).

Several methods for gas recovery from NGHs have been proposed, which mainly includes depressurization, thermal stimulation, inhibitor injection, and carbon dioxide replacement (Wang et al., 2014; Nandanwar et al., 2016; Liu et al., 2017). Among the methods mentioned above, the depressurization method is the most economical and effective one (Lee et al., 2011; Konno et al., 2016). As a consequence, the depressurization method has been adopted in field productions of NGHs in the Messoyakha gas field (Krason, 2000), the North Slope of Alaska (Schoderbek et al., 2013), the Nankai Trough in Japan Sea (Cyranoski, 2013; Yamamoto et al.,

*Corresponding author. E-mail: liulele_leo@163.com

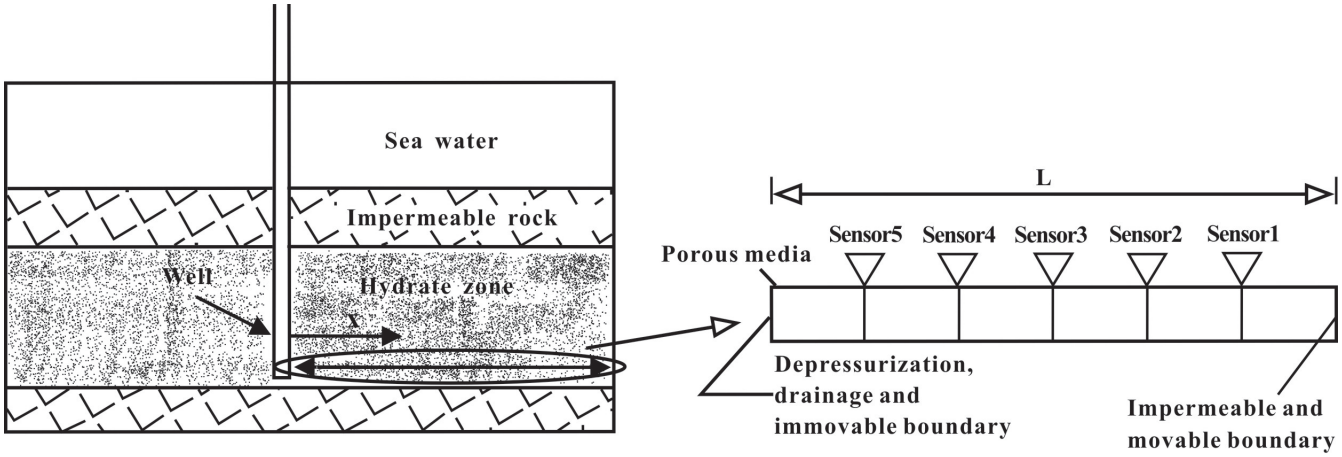

Fig. 1. Hydrate production induced by depressurization using a vertical well in marine sediments.

2014), and the Shenhu Area in South China Sea. Solid NGHs are decomposed into liquid water and natural gas during depressurization. This, in turn, may result in a loss of cementation and a corresponding effective stress decrease of hydrate-bearing sediments (HBS) (Hyodo et al., 2013; Song et al., 2014; Yoneda et al., 2015; Kajiyama et al., 2017; Zhang et al., 2017). NGHs have been treated as a potential trigger in submarine geohazards such as wellbore failures, seabed settlements, and submarine landslides (Nixon and Grozic, 2007; Lee et al., 2010b; Maslin et al., 2010; Ning et al., 2012). Therefore, a thorough understanding of deformation characteristics of HBS during depressurization is of great importance for stability analyses under different environmental conditions (Miyazaki et al., 2011; Ghiassian and Grozic, 2013; Zhang et al., 2015).

A vast variety of triaxial shear tests have been performed on HBS to understand the stress-strain behavior under different hydrate saturations (Yun et al., 2007; Miyazaki et al., 2011; Zhang et al., 2012; Ghiassian and Grozic, 2013; Hyodo et al., 2013; Hyodo et al., 2014; Li et al., 2016). Based on these experimental data, various constitutive models of HBS have been proposed and improved (Pinkert and Grozic, 2014; Lin et al., 2015; Pinkert et al., 2015; Sun et al., 2015; Shen et al., 2016; Uchida et al., 2016). Developing multi-field coupling numerical simulators with different constitutive models has been treated as an essential for analyzing mechanical responses of hydrate-bearing reservoirs during depressurization. Gupta et al. (2017) developed a simplified geomechanics-to-fluid coupling numerical simulator to study the impact of geomechanics on the hydrate dissociation behavior within cylindrical samples under triaxial shear condition. In the model, a linear-elastic constitutive model of HBS was applied. Chejara et al. (2013) applied a numerical simulator named RetrasoCode-Bright to study the long term hydrate production behavior during depressurization in Mount Elbert hydrate-bearing deposits, particularly the effective stress field. Cheng et al. (2013) established a fluid-solid coupling numerical simulator to imitate the depressurization-induced hydrate dissociation process within hydrate reservoirs, and the fluid-solid coupling effect was basically discussed. Kim et al. (2012) performed a case study of hydrate production in the Prudhoe Bay Unit L-Pad on the North Slope through numerical simulations. Different coupling models between fluid flow and geomechanics were compared and discussed. Kimoto et al. (2010) developed a chemo-thermo-mechanical numerical simulator to predict the deformation of hydrate reservoirs during hydrate dissociation induced by depressurization and thermal stimulation. A numerical simulator which combines TOUGH+HYDRATE and FLAC3D was commonly used to study the gas production behavior as well as the geomechanical response during hydrate recovery (Rutqvist and Moridis, 2008; Rutqvist et al., 2009).

In this paper, a Gas Hydrate Production Coupled Fluid-Solid-Heat Numerical Simulator (GrapeFloater) is firstly proposed, taking intrinsic kinetics of hydrate decomposition, two-phase fluid flow, conductive-convective heat transfer, and especially solid skeleton deformation into account for behaviors of hydrate dissociation in porous media. Then, a depressurization-induced hydrate dissociation experiment is performed, and the experimental results are used to validate the numerical simulator. Finally, a detailed sensitivity analysis is performed to discuss the deformation characteristic during depressurization.

2. Numerical model description

Figure 1 is a schematic diagram of hydrate production induced by depressurization using a vertical well in marine sediments. The circle part of cylindrical model showed on the left-hand side of figure 1 can be simplified into a one-dimensional model showed on the right-hand side of figure 1 on account of the axial symmetry. In the one-dimensional model, length of the porous media is expressed as *L*. The vertical well is located at $x = 0$. The well pressure is depressurized from P_e to P_0 in a brief period. At $x = L$, the boundary condition is assumed to be impermeable. Temperatures at both boundaries ($x = 0, x = L$) are fixed at T_e. Solid skeleton of the porous media is immovable at $x = 0$, but movable at $x = L$. Several assumptions considered by the numerical simulator are showed as follows:

a) Gas is consisted of pure methane, and the mass dissolved in water can be neglected.
b) There is no ice phase during the whole dissociation process.
c) The horizontal total stress of hydrate reservoir is unchanged.
d) The side friction forces of the porous media are neglected.

Mass conservation equations of gas, water, MH and solid skeleton are described as follows respectively.

$$\frac{\partial}{\partial t}\left(\varepsilon_g \rho_g\right)+\frac{\partial}{\partial x}\left(\rho_g U_g\right)=\dot{m_g} \tag{1}$$

$$\frac{\partial}{\partial t}\left(\varepsilon_w \rho_w\right)+\frac{\partial}{\partial x}\left(\rho_w U_w\right)=\dot{m_w} \tag{2}$$

$$\frac{\partial}{\partial t}\left(\varepsilon_h \rho_h\right)=-\dot{m_h} \tag{3}$$

$$\frac{\partial}{\partial t}\left(\varepsilon_s \rho_s\right)+\frac{\partial}{\partial x}\left(\rho_s u_s\right)=0 \tag{4}$$

Two-phase fluid flow satisfies the Darcys law:

$$U_g-u_s=-\frac{k_{rg}K}{\mu_g}\frac{\partial P_g}{\partial x} \tag{5}$$

$$U_w-u_s=-\frac{k_{rw}K}{\mu_w}\frac{\partial P_w}{\partial x} \tag{6}$$

where U is fluid velocity; u_s is horizontal deformation velocity of solid skeleton; ε is phase volume fraction; P is pore pressure; μ is viscosity; K is the absolute permeability of hydrate-bearing porous media; k_{rw} and k_{rg} are relative permeabilities of water and methane gas respectively; subscripts *g, w, h, s* stand for gas, water, MH and solid skeleton phase respectively. The four-phase volume fraction meets the following equation.

$$\varepsilon_g+\varepsilon_w+\varepsilon_h+\varepsilon_s=1 \tag{7}$$

μ_g is calculated by (Selim and Sloan, 1989).

$$\begin{aligned}\mu_g=&2.45\times10^{-6}+2.88\times10^{-8}T+3.28\times10^{-12}T^2\\&-3.78\times10^{-15}T^3+2.09\times10^{-8}\rho_g+2.51\times10^{-10}{\rho_g}^2\\&-5.82\times10^{-13}{\rho_g}^3+1.84\times10^{-16}{\rho_g}^4\end{aligned} \tag{8}$$

Pore pressures of water and methane gas are connected by the capillary pressure p_c.

$$p_c=P_g-P_w \tag{9}$$

The absolute permeability of hydrate-bearing porous media is calculated by (Kleinberg et al., 2003).

$$K=K_0(1-S_h)^N=K_0\left(1-\frac{\varepsilon_h}{1-\varepsilon_s}\right)^N \tag{10}$$

where K_0 is the absolute permeability of porous media without MH; N is permeability reduction index.

Relative permeabilities and capillary pressure are calculated based on Coreys model and can be expressed as follows (Sun et al., 2005).

$$k_{rg}=\left(\frac{\frac{S_g}{S_g+S_w}-S_{gr}}{1-S_{wr}-S_{gr}}\right)^{n_g}=\left(\frac{\frac{\varepsilon_g}{\varepsilon_g+\varepsilon_w}-S_{gr}}{1-S_{wr}-S_{gr}}\right)^{n_g} \tag{11}$$

$$k_{rw}=\left(\frac{\frac{S_w}{S_g+S_w}-S_{wr}}{1-S_{wr}-S_{gr}}\right)^{n_w}=\left(\frac{\frac{\varepsilon_w}{\varepsilon_g+\varepsilon_w}-S_{wr}}{1-S_{wr}-S_{gr}}\right)^{n_w} \tag{12}$$

$$p_c={p_c}^*\left(\frac{\frac{S_w}{S_g+S_w}-S_{wr}}{1-S_{wr}}\right)^{-n_c}={p_c}^*\left(\frac{\frac{\varepsilon_w}{\varepsilon_g+\varepsilon_w}-S_{wr}}{1-S_{wr}}\right)^{-n_c} \tag{13}$$

where S_{gr} and S_{wr} are residual saturations of methane gas and water respectively; p_c^* is the nominal capillary pressure; n_g , n_w , and n_c are empirical constants.

Total stress of hydrate-bearing porous media is expressed as follow.

$$\sigma_e+\frac{\varepsilon_g}{\varepsilon_g+\varepsilon_w}P_g+\frac{\varepsilon_w}{\varepsilon_g+\varepsilon_w}P_w=\sigma \tag{14}$$

The hydrate-bearing porous media is assumed to be elastic, which is:

$$\sigma_e=-E\frac{\partial l}{\partial x} \tag{15}$$

Time derivative of effective stress can be obtained from Eq. 15, which is:

$$\frac{\partial\sigma_e}{\partial t}=-E\frac{\partial u_s}{\partial x}=\frac{\partial}{\partial t}\left(\sigma-\frac{\varepsilon_g}{\varepsilon_w+\varepsilon_g}P_g-\frac{\varepsilon_w}{\varepsilon_w+\varepsilon_g}P_w\right) \tag{16}$$

in which σ is total stress; σ_e is effective stress; E is modulus of hydrate-bearing porous media; l is the horizontal deformation of porous media.

The energy balance relationship is showed in Eq. 17. Both conductive and convective heat transfer are considered. On the right-hand side of the equation, the first term is the energy consumption in terms of hydrate dissociation, and the second term is the energy input from surrounding environment which has an unchanged temperature T_e.

$$\begin{aligned}&\left(\varepsilon_g\rho_g C_g+\varepsilon_h\rho_h C_h+\varepsilon_w\rho_w C_w+\varepsilon_s\rho_s C_s\right)\frac{\partial T}{\partial t}+\\&\left(\rho_g U_g C_g+\rho_w U_w C_w+\rho_s u_s C_s\right)\frac{\partial T}{\partial x}-\frac{\partial}{\partial x}\left(\lambda\frac{\partial T}{\partial x}\right)\\&=\left[\frac{\partial\left(\rho_h\varepsilon_h\right)}{\partial t}\right]\Delta H+\dot{q_{in}}\end{aligned} \tag{17}$$

where T is temperature, C is heat capacity, $\dot{q_{in}}$ is the rate of heat transfer from outside into porous media per unit volume, λ is thermal conductivity of hydrate-bearing porous media which is defined as follow.

$$\lambda=\varepsilon_g\lambda_g+\varepsilon_w\lambda_w+\varepsilon_h\lambda_h+\varepsilon_s\lambda_s \tag{18}$$

ΔH is the latent heat (enthalpy change during MH decomposition) which can be expressed as follow.

$$\Delta H=3.53\times10^6-1.05\times10^3T \tag{19}$$

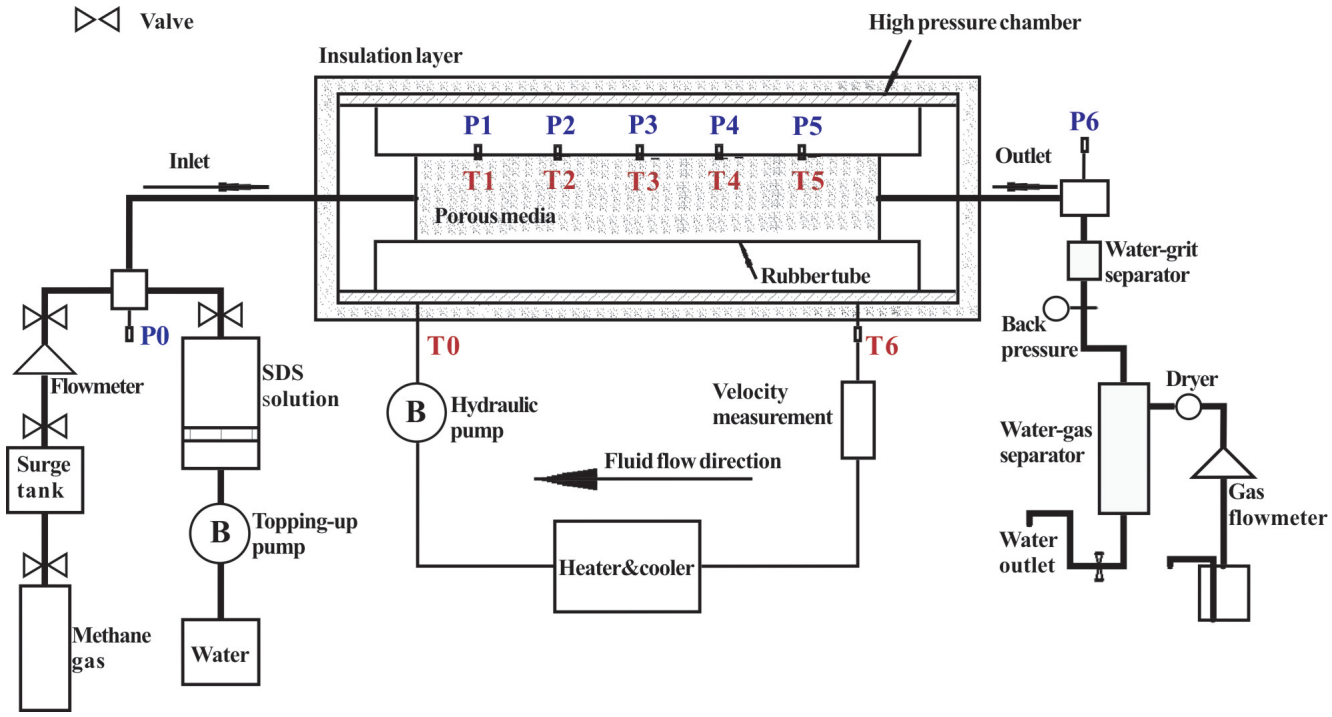

Fig. 2. Experimental apparatus for hydrate production.

According to the molecular formula of MH, the following equations can be derived.

$$\dot{m}_h = \dot{m}_g \frac{N_H M_w + M_g}{M_g} \tag{20}$$

$$\dot{m}_w = \dot{m}_g \frac{N_H M_w}{M_g} \tag{21}$$

The hydrate dissociation process is controlled by the Kim-Bishnoi model (Kim et al., 1987) which is:

$$\dot{m}_g = k_d M_g A_s \left(f_e - f\right) \tag{22}$$

where f_e and f are equilibrium reaction fugacity and gas fugacity, which can be replaced by equilibrium pressure p_{eq} and local gas pressure P_g respectively. The equilibrium pressure is calculated by (Selim and Sloan, 1989):

$$p_{eq} = \exp\left(49.3 - \frac{9.46 \times 10^3}{T}\right) \tag{23}$$

k_d is the MH dissociation coefficient which can be calculated by:

$$k_d = k_0 \exp\left(-\frac{\Delta E}{RT}\right) \tag{24}$$

in which k_0 is the intrinsic rate constant of MH decomposition; ΔE is the active energy of MH dissociation; R is gas constant.

In Eq. 22, A_s is interface area between MH and fluid phase which can be calculated in the following way.

$$A_s = \sqrt{\frac{\left(\phi_{wg}\right)^3}{2K}} \tag{25}$$

$$\phi_{wg} = \phi\left(1 - S_h\right) = \varepsilon_g + \varepsilon_w \tag{26}$$

Initial conditions are as follows:

$$P_g = P_e, T = T_e, \varepsilon_g = \varepsilon_g^0, \varepsilon_w = \varepsilon_w^0, \varepsilon_h = \varepsilon_h^0,$$
$$\varepsilon_s = \varepsilon_s^0, U_g = 0, U_w = 0, u_s = 0, l = -(\sigma_e^0/E)x$$
$$for\ 0 \leqslant x \leqslant L\ and\ t = 0$$

Boundary conditions are given below:

$$P_g = P_0, T = T_e, l = 0, for\ x = 0\ and\ t \geqslant 0$$
$$\frac{\partial P_g}{\partial x} = 0, T = T_e, for\ x = L\ and\ t \geqslant 0$$

3. Experimental apparatus and materials

Sketch of the experimental apparatus is shown in Fig. 2. A cylindrical sample with a diameter of 3.8 cm and a length of 78 cm is wrapped by a rubber tube. Both the sample and the tube are put in a stainless steel chamber. Low-temperature fluid is introduced into the annular space between the rubber and the chamber to cool the system and provide confining pressure during experiments. Five pore pressure transducers (P1∼T5) and temperature sensors (T1∼T5) are placed along the axial direction in a 13 cm interval. Pore pressure transducers P0 and P6 are used to measure the pressures of inlet and outlet respectively. Temperature sensors T0 and T6 are installed to measure the fluid temperatures through the input and output respectively. Thermal insulating material wrapped the pressure chamber is used to prevent the heat diffusion.

Table 1. Numerical initial conditions obtained from the hydrate dissociation experiment.

Parameter	Value	Parameter	Value
Volume fraction of skeleton, ε_s^0	0.657	Pore pressure, $P_e(MPa)$	3.5
Volume fraction of hydrate, ε_h^0	0.203	Temperature, $T_e(K)$	275
Volume fraction of water, ε_w^0	0.077	Well pressure, $P_0(MPa)$	0.1
Volume fraction of gas, ε_g^0	0.063	Sample length, $L(m)$	0.78
Absolute permeability without MH, $K_0(md)$	150	Sample diameter, $D(m)$	0.038
Total stress, $\sigma(MPa)$	6.0	Antifreeze fluid temperature, $T_e(K)$	275

Table 2. Parameters used in the numerical model.

Parameter	Value	Parameter	Value
Specific heat of glass beads, $C_s(kJ/kg/K)$	0.89	Permeability reduction index, N	5.0
Specific heat of MH, $C_h(kJ/kg/K)$	2.22	Empirical constant used in Eq.(14), n_g	2.0
Specific heat of water, $C_w(kJ/kg/K)$	4.2	Empirical constant used in Eq.(15), n_w	4.0
Specific heat of gass, $C_g(kJ/kg/K)$	2.18	Empirical constant used in Eq.(16), n_c	0.65
Density of glass beads, $\rho_s(kg/m^3)$	2600	Residual saturation of methane gas, S_{gr}	0.02
Density of MH, $\rho_h(kg/m^3)$	910	Residual saturation of water, S_{wr}	0.2
Density of water, $\rho_w(kg/m^3)$	1000	Nominal capillary pressure, $p_c^*(kPa)$	4
Thermal conductivity of glass beads, $\lambda_s(W/m/K)$	2.9	Intrinsic rate constant of hydrate decomposition, $k_0(kmol/m^2/Pa/s)$	36
Thermal conductivity of hydrate, $\lambda_h(W/m/K)$	0.46	Active energy of MH dissociation, $\triangle$E(kJ)	81
Thermal conductivity of water, $\lambda_w(W/m/K)$	0.56	Deformation modulus of MH stratum, $E(GPa)$	10
Thermal conductivity of gas, $\lambda_g(W/m/K)$	0.07	Thickness of rubber tube, $d(m)$	0.008
Viscosity of water, $\mu_w(cp)$	1.0	Thermal conductivity of rubber tube, $\lambda_e(W/m/K)$	0.26

Glass beads with grain sizes between 250 μm and 420 μm are used to form host porous media. Methane gas with a purity of 99.9% and distilled water are used to form MH within the host porous media. The partial water saturation method (Ghiassian and Grozic, 2013) is applied to form hydrate, and the depressurization method is subsequently used to decompose hydrate. Annealing process (Lee et al., 2010a) is performed several times to enhance the homogeneity of hydrate distribution within porous media. During the experiment, temperature, pore pressure, injected and produced gas volumes as well as produced water volume are recorded every five seconds using a data acquisition system.

4. Model validation and numerical results

Glass beads sample under a confining pressure of 6 MPa is assumed to be rigid and fixed. The initial conditions for the numerical simulator shown in Table 1 were determined from the hydrate formation and dissociation experiment, and parameters applied in the numerical simulator are shown in Table 2.

The model of heat transfer between the antifreeze fluid and the rubber tube is assumed to be conductive on account of the low-velocity of antifreeze fluid flow in the annular space (about 0.2 cm/s). Hence, the rate of heat transfer per unit volume in Eq. 17 can be written as follow:

$$\dot{q_{in}} = \frac{4}{D}\lambda_e \frac{T_e - T}{d} \tag{27}$$

where *D* is diameter of the sample; *d* is thickness of the rubber tube; λ_e is thermal conductivity of the rubber tube.

Figure 3 shows the cumulative produced gas volume over time. In the figure, the experimental data are shown as dots and the solid black line stands for the numerical model fitting result. Maximum of cumulative produced gas volume predicted by the numerical model is 30.7 standard liters which is quite closed to 31.2 standard liters measured in the experiment. It is obvious that the numerical simulator predicted curve fits the experimental data relatively well, which demonstrates the feasibility of the numerical simulator.

Figure 4 shows gas pressures of sensor 4 and 2 over time. In the figure, pressure of sensor 4 decreases much earlier than that of sensor 2. Moreover, pressure of sensor 2 needs much longer time than that of sensor 4 to decrease entirely. At the beginning of hydrate dissociation, pressure predicted by the numerical simulator drops down much earlier than that measured in the experiment. However, predicted pressure need more time to decrease entirely than experimental pressure. Dri-

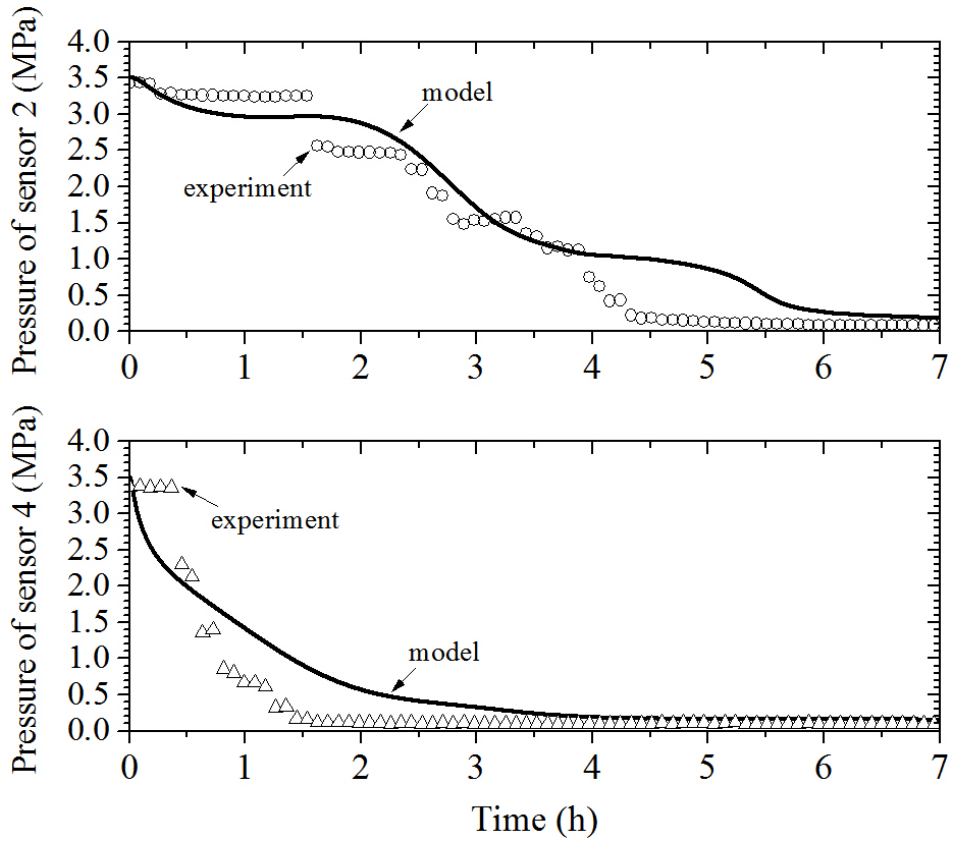

Fig. 4 . Gas pressures of sensors 2 and 4 over time.

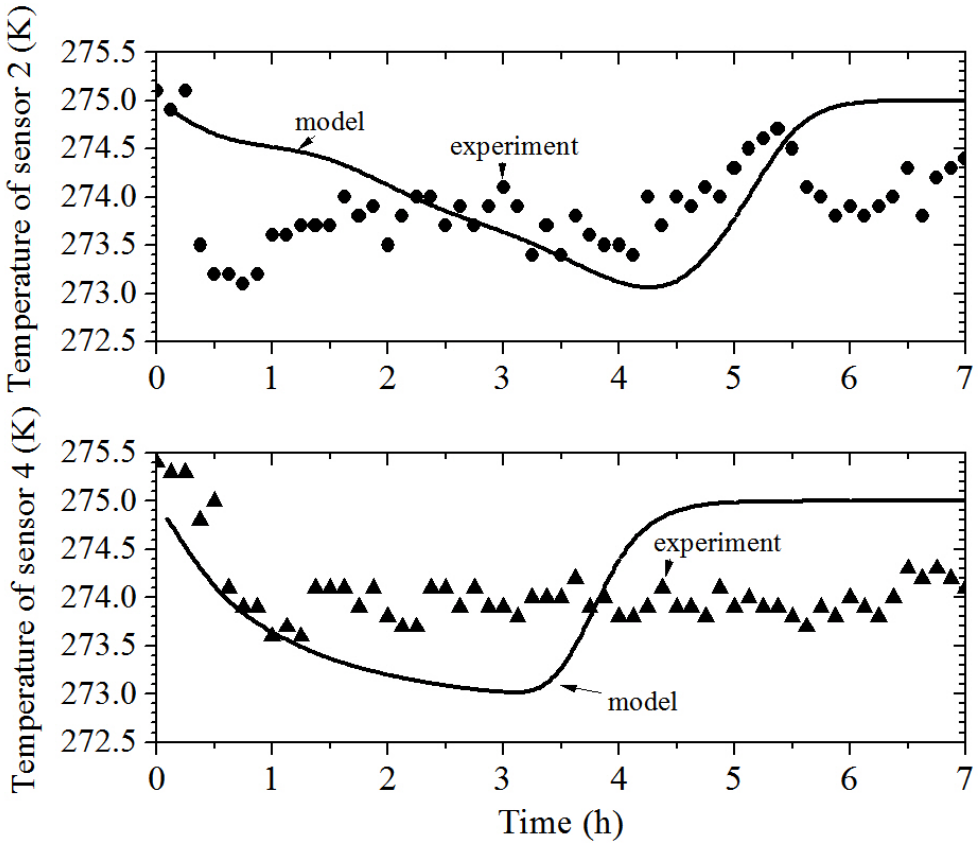

Fig. 5 . Temperatures of sensors 2 and 4 over time.

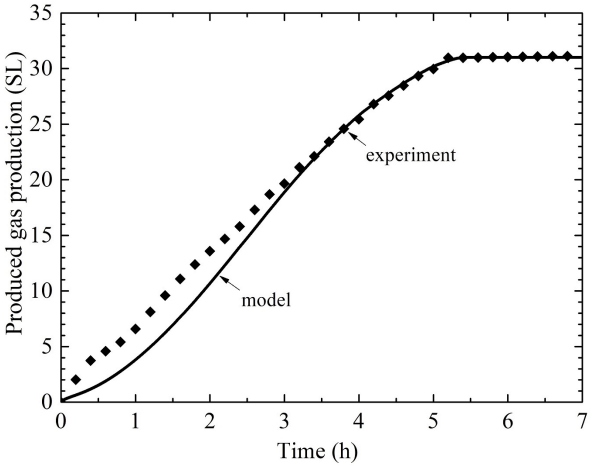

Fig. 3 . Cumulative produced gas volume over time.

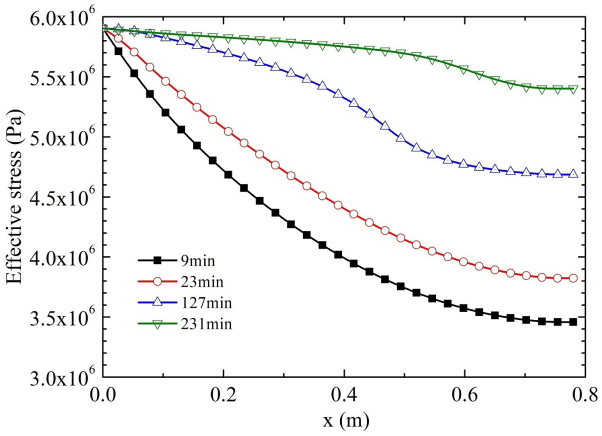

Fig. 7. Effective stress during dissociation at different times.

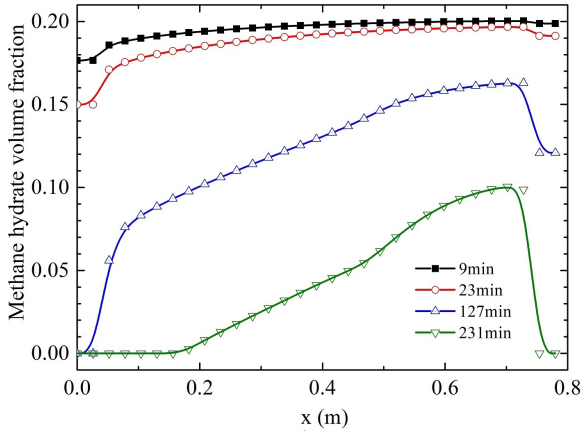

Fig. 6. MH volume fraction during dissociation at different times.

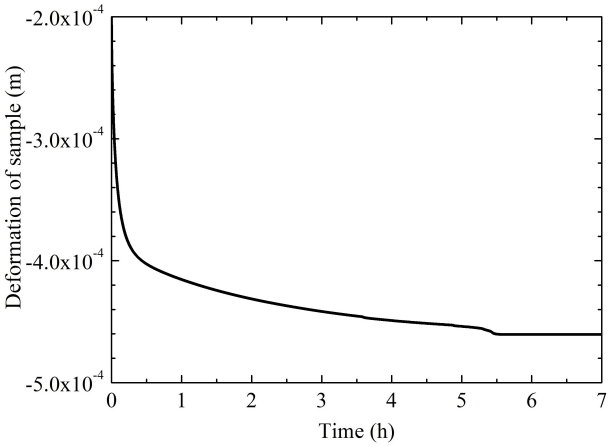

Fig. 8. Deformation at x=L during dissociation.

ving pressure force and heat supply condition near the outlet are the best, and those near the inlet are a little worse. In addition, driving pressure force and heat supply condition in the middle of sample are the worst. As a consequence, hydrate dissociation rate near the outlet is the largest, and the hydrate dissociation rate in the middle of sample is the smallest. Hydrate dissociation enhances the permeability of hydrate-bearing porous media. Hence, the more quickly the hydrate dissociates, the more quickly the pressure drops down. The numerical model is developed based on the homogenous assumption, but the hydrate distribution within the sample is heterogeneous. This may cause the pore pressure differences between predicted curve and experimental data.

Figure 5 shows temperatures of sensor 2 and 4 over time. In the figure, temperature of sensor 4 decreases to the lowest value a little earlier than that of sensor 2. This is because that MH at sensor 4 dissociates earlier than that at sensor 2. The maximum of temperature decrease of sensors 2 is different from that of sensor 2, and the experimental temperatures are lower than predicted temperatures at the latter period of experiment. These may be caused by the heterogeneous of hydrate distribution with porous media.

Figures 6 and 7 show the MH volume fraction and effective stress at t = 9, 23, 127 and 231 minutes respectively. In figure 6, the dissociation rate of MH near the depressurized outlet is larger than that of MH far from the depressurized outlet. However, the dissociation rate of MH at the opposite side (0.7∼0.78 m) of the depressurized outlet becomes faster at the latter period of the dissociation process. There is no obvious MH dissociation front. It is inferred that MH can only dissociate progressively from the depressurized outlet if the permeability of the sample is small enough. In figure 7, the effective stress increases with time because of the reduction of pore pressure. The pore pressure increases when the gas-fluid velocity is larger than the gas-production rate, but decreases when the gas-fluid velocity is smaller than the gas-production rate. It suggests that the gas permeability of sample is large enough that the gas produced from MH dissociation can flow out of the sample easily.

Figure 8 shows the deformation at $x = L$ during the MH

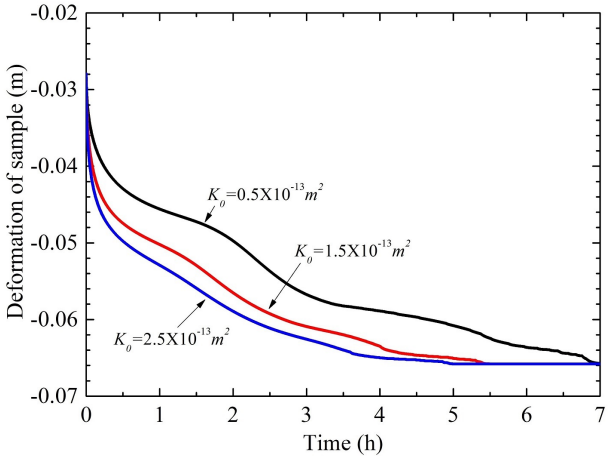

Fig. 9. Deformations at different absolute permeability cases.

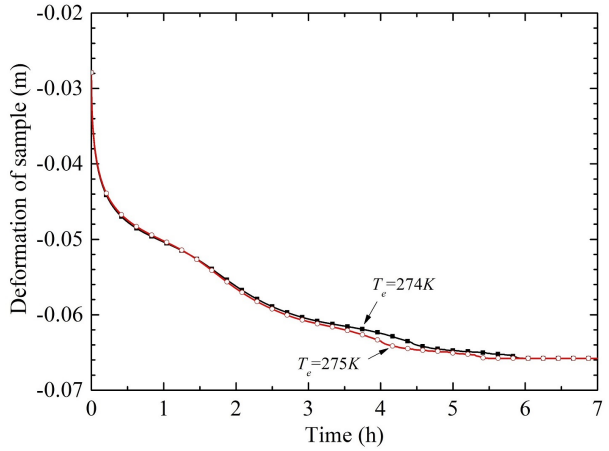

Fig. 10. Deformations at different environmental temperature cases.

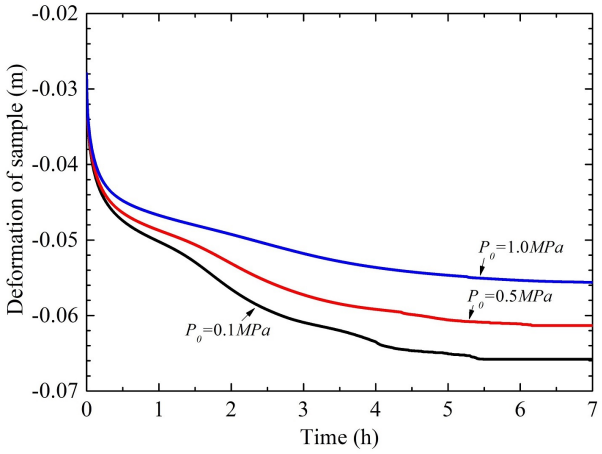

Fig. 11. Deformations at different outlet pressure cases.

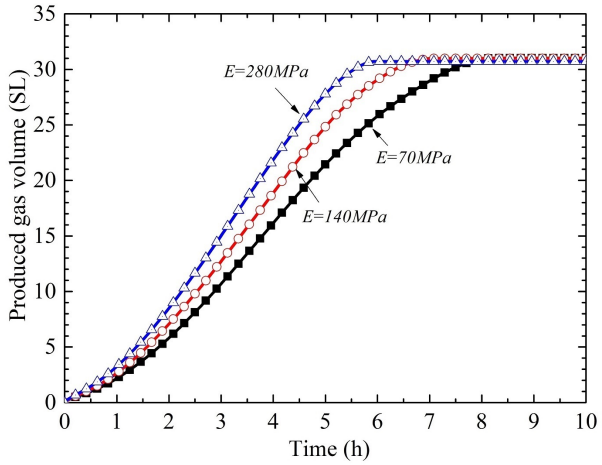

Fig. 12. Produced gas productions at different modulus cases.

dissociation. In this figure, negative values of deformation mean that the sample is compressive. The initial deformation of sample is -0.0002 m which is caused by the initial effective stress. The deformation becomes larger during the MH dissociation because of the decrease of effective stress and pore pressure. The final deformation is -0.0005 m. It suggests that the deformation of sample caused by MH dissociation is 0.04% of the sample length.

5. Sensitivity analysis

MH dissociation may destroys the structural integrity of hydrate-bearing porous media, MH dissociation may subsequently lead to a significant deformation, especially for fine-grained sediments. In this section, the deformation modulus used in the numerical model is adopted to be 70 MPa in order to simulate the MH dissociation process in the fine-grained sample. Parameters sensitivity analyses are developed as follows.

5.1 Geomechanical response of fine-grained sample

The geomechanical responses of fine-grained sample mainly include changes of porosity, modulus, effective stress and deformation. The deformation of fine-grained sample is the most important parameter on account of its great significance for the safety analysis. The absolute permeability, environmental temperature and outlet pressure are discussed as follows to analysis their effects on the deformation behavior.

a) Absolute permeability

Figure 9 shows the deformation at $x=L$ at different absolute permeability cases. Final deformations in these three cases are the same, but the deformation duration decreases with increasing absolute permeability. This is because that the two-phase fluid flows faster and the rate of pore pressure decrease and effective stress increase becomes lager at higher absolute permeability. The pressure driving force for MH dissociation also increases with increasing absolute permeability.

b) Environmental temperature

Figure 10 shows the deformation at $x=L$ at different environmental temperatures. Final deformations of these two cases

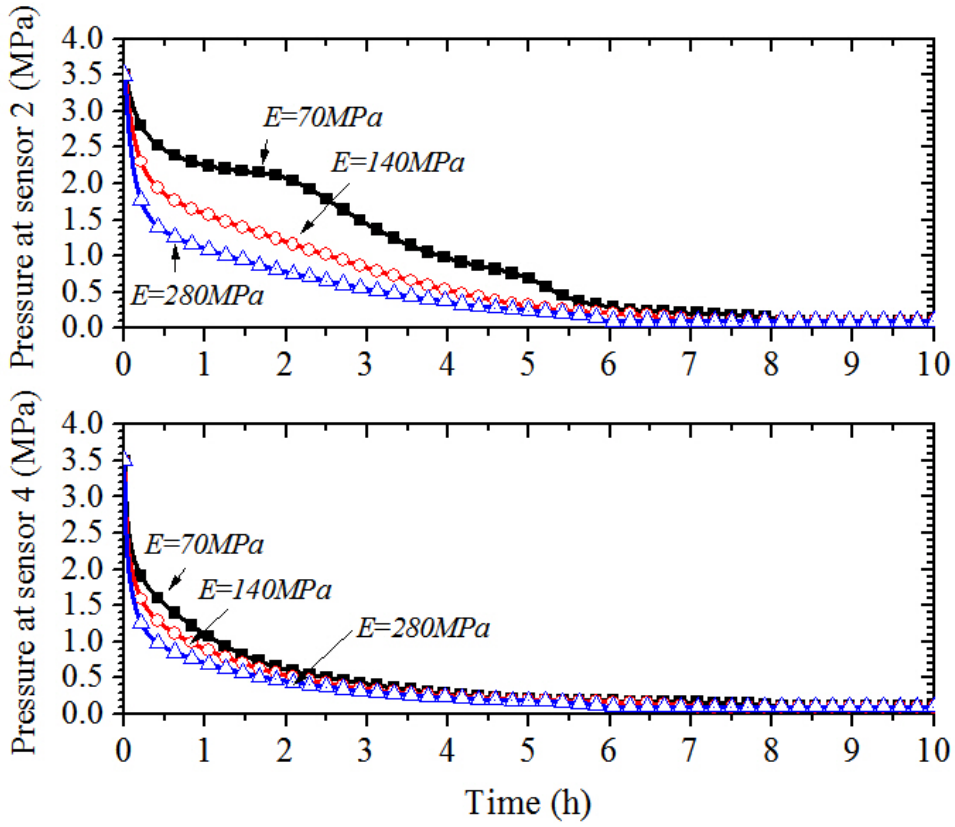

Fig. 13. Pressures at sensor 4 and 2 at different modulus cases.

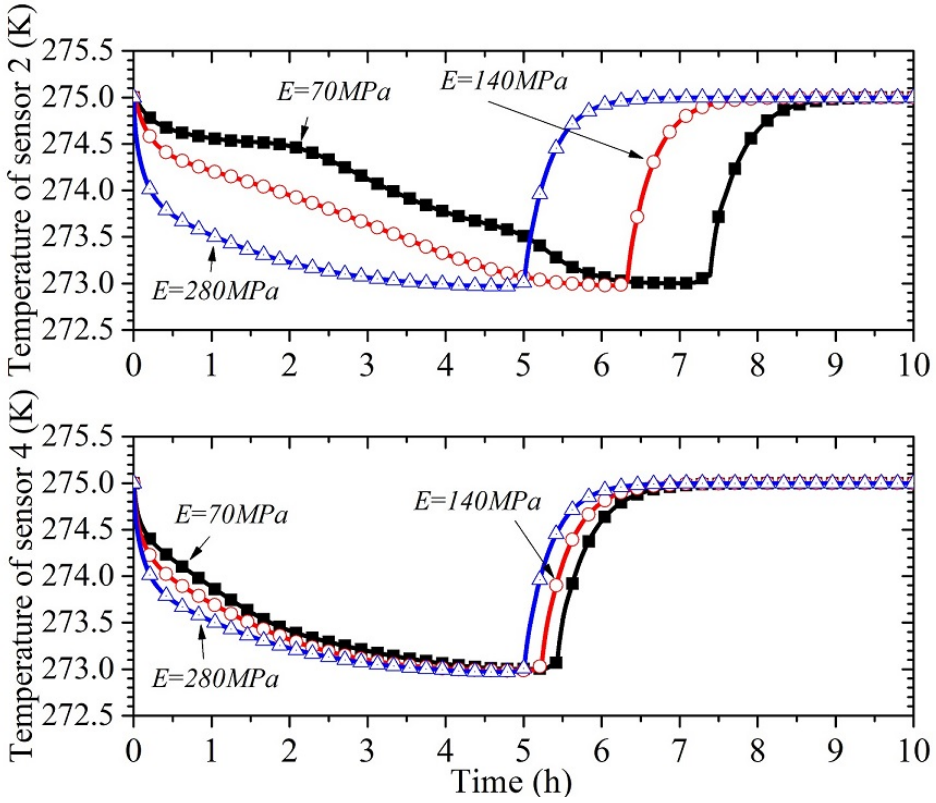

Fig. 14. Temperatures at sensor 4 and 2 at different modulus cases.

are the same. The increasing environmental temperature leads to the decrease of deformation duration. The reason is that the MH dissociation becomes faster with a higher environmental temperature.

c) Outlet pressure

Figure 11 shows the deformation at $x=L$ at different outlet pressures. Final deformations of outlet pressures at 0.1 MPa, 0.5 MPa and 1.0 MPa are -0.066 m, -0.061 m and -0.056 m respectively. It means that the deformation decreases with increasing outlet pressure. This is because that increasing outlet pressure leads to the decrease of effective stress which causes less deformation. Moreover, the whole deformation process lasts longer time when the outlet pressure is higher, which is on account of the decreasing pressure driving force for hydrate dissociation.

5.2 Hydrate production behavior

The deformation of the fine-grained sample affects the behavior of two-phase fluid flow, conductive-convective heat transfer and intrinsic kinetics of hydrate dissociation. The modulus of the solid skeleton is one of the key factors which affect the deformation. Because the cumulative gas production, pressure, and temperature are important factors for analyzing hydrate dissociation process, these three parameters are chosen as the aim to investigate the modulus sensitivity analysis.

a) Cumulative gas production

Figure 12 shows the produced gas volume at different modulus cases. Final produced gas volumes of these three cases are the same, but the whole gas production process lasts longer time when the modulus is lower. This in turn suggests that hydrate dissociates more quickly with a higher modulus.

b) Pressure

Figure 13 shows the pressures of sensor 4 and 2 at different modulus cases. Pressures of sensor 4 and 2 decrease more quickly with higher modulus, and the whole pressure reduction process lasts longer with lower modulus. This also suggests that hydrate dissociates more quickly with a higher modulus.

c) Temperature

Figure 14 shows the temperatures of sensor 4 and 2 at different modulus cases. Temperatures of sensor 4 and 2 decrease more quickly with a higher modulus, and the whole temperature change process lasts longer when the modulus is lower. The increasing modulus leads to increasing maximum temperature decrease. This suggests that hydrate dissociates more quickly when the modulus is higher too.

Volume fraction of solid skeleton increases with decreasing modulus of hydrate-bearing porous media. On the contrary, the mobility of two-phase fluid as well as the pressure decrease rate decreases with decreasing modulus of hydrate-bearing porous media. The driving pressure force for MH dissociation decreases when the pressure decrease rate is decreasing. Hence, hydrate dissociates more quickly when the modulus is higher.

6. Discussions

Figure 15 shows the deformation at $x=L$ at different modulus cases. Initial deformations of moduli at 70 MPa, 140 MPa and 280 MPa are -0.028 m, -0.014 m and -0.007 m respectively. Final deformations of these moduli are -0.066 m, -0.036 m and -0.016 m. Deformations caused by MH dissociation of these three moduli are -0.038 m, -0.022 m and -0.009 m. The deformation duration decreases with increasing modulus. This is because that gas produced from hydrate can flow out of the sample easily at this condition. Consequently, the deformation duration is equal to the MH dissociation duration. The volume fraction of solid skeleton becomes larger with lower modulus of porous media. The mobility of two-phase fluid, the decrease rate of pore pressure, and the driving pressure force for hydrate dissociation decrease with decreasing modulus. In a word, the MH dissociation process lasts longer when the modulus of hydrate-bearing porous media is smaller.

In Fig. 15, deformations of hydrate-bearing porous media are calculated by assuming that the modulus is a constant during hydrate dissociation. However, the modulus decreases during hydrate dissociation, and the modulus of hydrate-

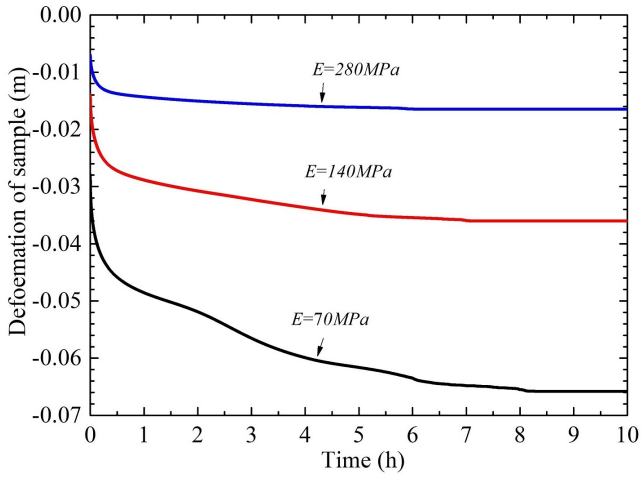

Fig. 15. Time evolution of deformation at different modulus cases.

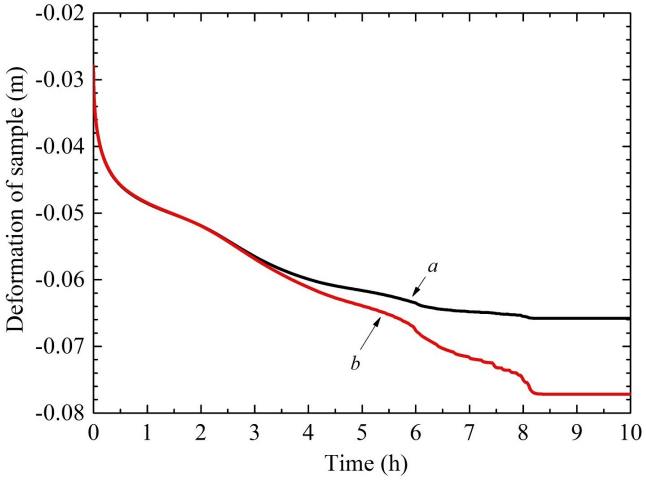

Fig. 16. Time evolution of deformation for different modulus cases.

bearing porous media is assumed to be:

$$E = E_0 + \frac{\varepsilon_h(1-\varepsilon_s^0)}{\varepsilon_h^0(1-\varepsilon_s)}E' \tag{28}$$

where E_0 is 13 MPa and E' is 57 MPa. In Fig. 16, line a is the deformation at x=L at the constant-modulus condition, and line b is the result computed with Eq. 28. The deformation at x=L of line b is -0.077 m which is larger than that of line a. Deformations of these two cases are the same at the front part of deformation duration, but the difference between these two cases increases later. This is because that the modulus decrease is small at the beginning. However, the modulus decrease becomes more obviously at the later period of hydrate dissociation.

7. Conclusions

In this study, a numerical simulator named GrapeFloater is developed. Then, a depressurization experiment is performed to validate the numerical simulator. A detailed parameter sensitivity analysis is finally carried out to study the deformation behavior of hydrate-bearing porous media. Main conclusions can be drawn as follows:

The numerical simulator is feasible, which can capture the deformation behavior of hydrate-bearing porous media during depressurization. The modulus of hydrate-bearing porous media has little effect on the final produced gas volume, but has obvious effect on produced gas velocities, pore pressures, and temperatures.

The deformation rate increases with increasing absolute permeability and increasing environmental temperature as well as decreasing outlet pressure. Final deformation does not change with absolute permeability and environmental temperature, but decreases when the outlet pressure is increasing. The pressure decrease caused by depressurization contributes to the deformation of hydrate-bearing porous media, and the modulus decrease caused by hydrate dissociation promotes the deformation.

Nomenclature

x=Spatial variable along the one-dimensional model in figure 1, m

L=length of the one-dimensional model in figure 1, m

P_e=Initial pore pressure of hydrate-bearing porous media, Pa

P=Pore pressure of hydrate-bearing porous media, Pa

P_0=Well pressure during depressurization, Pa

T_e=Environmental temperature of the one-dimensional model, K

T=Temperature of hydrate-bearing porous media, K

ε=Volume fraction

ε^0=Initial volume fraction

ρ=Density, kg/m^3

t=elapsed time, s

U=Seepage velocity, m/s

m=Rate of local mass changed induced by hydrate dissociation, kg/m^3·s

u=Deformation velocity, m/s

k_r=Relative permeability

K=Absolute permeability of hydrate-bearing porous media, m^2

K_0=Absolute permeability of hydrate-free porous media, m^2

μ=Viscosity coefficient, $Pa \cdot s$

p_c=Capillary pressure, Pa

p_c^*=Nominal capillary pressure, Pa

S=Saturation

S_r=Residual saturation

N=Permeability reduction index

n_g, n_w, n_c=Empirical constants of the Coreys Model

σ_e=Effective stress, Pa

σ=Total stress, Pa

E=Modulus of hydrate-bearing porous media, Pa

I=Deformation of hydrate-bearing porous media, m

C=Specific heat capacity, $J/kg \cdot K$

λ=Thermal conductivity, $J/m \cdot K$

$\triangle$H=Latent heat of hydrate dissociation, J/kg

q_{in}=Heat transfer rate, $J/m^3 \cdot s$

M=Molecular weight, kg/mol

N_H=Hydrate number

k_d=Hydrate dissociation coefficient, $kg/m^2 \cdot Pa \cdot s$

k_0=Intrinsic rate constant of hydrate dissociation, $kg/m^2 \cdot Pa \cdot s$

A_s=Area of hydrate dissociation per unit volume, m^{-1}

f_e=Equilibrium reaction fugacity, Pa

f=Gas fugacity, Pa

p_{eq}=Equilibrium pressure of hydrate, Pa

$\triangle$E=Active energy of hydrate dissociation, J/mol

R=Universal gas constant (=8.314 $J/mol \cdot K$)

ϕ=porosity

ϕ_{wg}=Effective porosity occupied by gas and water

D=Diameter of the experimental specimen, m

d=Thickness of the rubber tube, m

λ_e=Thermal conductivity of the rubber tube, $J/m \cdot K$

E_0=Deformation modulus of hydrate-free porous media, Pa

E'=Deformation modulus increase on account of hydrate, Pa

Subscripts and superscripts

g=methane gas

w=water

s=solid skeleton of hydrate-bearing porous media

h=methane hydrate

Acknowledgments

This work was supported by the National Science Foundation of China (No.11402131) and the China Geological Survey Project (DD20160216). They are gratefully acknowledged.

References

Boswell, R. Is gas hydrate energy within reach? Science 2009, 325(5943): 957-958.

Boswell, R., Collett, T.S. Current perspectives on gas hydrate resources. Energ. Environ. Sci. 2011, 4(4): 1206-1215.

Chejara, A., Kvamme, B., Vafaei, M.T., et al. Simulations of long term methane hydrate dissociation by pressure reduction using an extended RetrasoCodeBright simulator. Energ. Convers. Manage. 2013, 68(2013): 313-323.

Cheng, Y., Li, L., Yuan, Z., et al. Finite element simulation for fluid-solid coupling effect on depressurization-induced gas production from gas hydrate reservoirs. J. Nat. Gas. Sci. Eng. 2013, 10(0): 1-7.

Chong, Z.R., Yang, S.H.B., Babu, P., et al. Review of natural gas hydrates as an energy resource: Prospects and challenges. Appl. Energ. 2016, 162: 1633-1652.

Collett, T., Bahk, J.J., Baker, R., et al. Methane Hydrates in Nature-Current Knowledge and Challenges. J. Chem. Eng. Data. 2015, 60(2): 319-329.

Cyranoski, D. Japanese test coaxes fire from ice: first attempt to extract methane from frozen hydrates far beneath the ocean shows promise. Nature 2013, 496(7446): 409-410.

Ghiassian, H., Grozic, J.L.H. Strength behavior of methane hydrate bearing sand in undrained triaxial testing. Mar. Petrol. Geol. 2013, 43(0): 310-319.

Gupta, S., Deusner, C., Haeckel, M., et al. Testing a thermo-chemo-hydro-geomechanical model for gas hydrate-bearing sediments using triaxial compression laboratory experiments. Geochem. Geophy. Geosy. 2017, 18(9): 3419-3437.

Hyodo, M., Li, Y., Yoneda, J., et al. Effects of dissociation on the shear strength and deformation behavior of methane hydrate-bearing sediments. Mar. Petrol. Geol. 2014, 51: 52-62.

Hyodo, M., Li, Y., Yoneda, J., et al. Mechanical behavior of gas-saturated methane hydrate-bearing sediments. J. Geophys. Res-Sol. Ea. 2013, 118(10): 5185-5194.

Kajiyama, S., Wu, Y., Hyodo, M., et al. Experimental investigation on the mechanical properties of methane hydrate-bearing sand formed with rounded particles. J. Nat. Gas. Sci. Eng. 2017, 45: 96-107.

Kim, H.C., Bishnoi, P.R., Heidemann, R.A., et al. Kinetics of methane hydrate decomposition. Chem. Eng. Sci. 1987, 42(7): 1645-1653.

Kim, J., Moridis, G.J., Rutqvist, J., et al. Coupled flow and geomechanical analysis for gas production in the Prudhoe Bay Unit L-106 well Unit C gas hydrate deposit in Alaska. J. Petrol. Sci. Eng. 2012, 92: 143-157.

Kimoto, S., Oka, F., Fushita, T., et al. A chemo-thermo-mechanically coupled analysis of ground deformation induced by gas hydrate dissociation. Int. J. Mech. Sci. 2010, 52(2): 365-376.

Kleinberg, R., Flaum, C., Griffin, D., et al. Deep sea NMR: methane hydrate growth habit in porous media and its relationship to hydraulic permeability, deposit accumulation, and submarine slope stability. J. Geophys. Res. 2003, 108(B10): 2508.

Konno, Y., Masuda, Y., Akamine, K., et al. Sustainable gas production from methane hydrate reservoirs by the cyclic depressurization method. Energ. Convers. Manag. 2016, 108: 439-445.

Krason, J. Messoyakh gas field (W. Siberia): A model for development of the methane hydrate deposits of Mackenzie Delta. Ann. NY. Acad. Sci. 2000, 912(1): 173-188.

Lee, J., Park, S., Sung, W. An experimental study on the productivity of dissociated gas from gas hydrate by depressurization scheme. Energ. Convers. Manage. 2010a, 51(12): 2510-2515.

Lee, J.Y., Ryu, B.J., Yun, T.S., et al. Review on the gas hydrate development and production as a new energy resource. KSCE J. Civ. Eng. 2011, 15(4): 689-696.

Lee, J.Y., Santamarina, J.C., Ruppel, C. Volume change associated with formation and dissociation of hydrate in sediment. Geochem. Geophy. Geosy. 2010b, 11(3): Q03007.

Li, Y., Liu, W., Zhu, Y., et al. Mechanical behaviors of permafrost-associated methane hydrate-bearing sediments under different mining methods. Appl. Energ. 2016, 162: 1627-1632.

Lin, J.S., Seol, Y., Choi, J.H. An SMP critical state model for methane hydrate-bearing sands. Int. J. Numer. Anal. Met. 2015, 39(9): 969-987.

Liu, J., Shao, Z., Wu, M., et al. Heat and mass transfer analysis of depressurization-induced hydrate decomposition with different temperatures of over- and underburden. J. Nat. Gas. Sci. Eng. 2017, 44: 65-76.

Makogon, Y.F., Holditch, S.A., Makogon, T.Y. Natural gas-hydrates-A potential energy source for the 21st Century. J. Petrol. Sci. Eng. 2007, 56(1-3): 14-31.

Maslin, M., Owen, M., Betts, R., et al. Gas hydrates: past and future geohazard? Philos. Trans. R. Soc. A: Math. Phy. Eng. Sci. 2010, 368(1919): 2369-2393.

Miyazaki, K., Masui, A., Sakamoto, Y., et al. Triaxial compressive properties of artificial methane-hydrate-bearing sediment. J. Geophys. Res-Sol Ea. 2011, 116(B6): B06102.

Nandanwar, M.S., Anderson, B.J., Ajayi, T., et al. Evaluation of gas production potential from gas hydrate deposits in National Petroleum Reserve Alaska using numerical simulations. J. Nat. Gas. Sci. Eng. 2016, 36: 760-772.

Ning, F., Yu, Y., Kjelstrup, S., et al. Mechanical properties of clathrate hydrates: status and perspectives. Energ. Environ. Sci. 2012, 5(5): 6779-6795.

Nixon, M.F., Grozic, J.L. Submarine slope failure due to gas hydrate dissociation: a preliminary quantification. Can. Geotech. J. 2007, 44(3): 314-325.

Pinkert, S., Grozic, J.L.H. Prediction of the mechanical response of hydrate-bearing sands. J. Geophys. Res-Sol. Ea. 2014, 119: 4695-4707.

Pinkert, S., Grozic, J.L.H., Priest, J.A. Strain-softening model for hydrate bearing sand. Int. J. Geomech. 2015, 15(6): 04015007

Rutqvist, J., Moridis, G. Coupled hydrologic, thermal and geomechanical analysis of well bore stability in hydrate-bearing sediments. Paper OTC19572 Presented at Offshore Technology Conference, Houston, Texas, USA, 5-8

May, 2008.

Rutqvist, J., Moridis, G.J., Grover, T., et al. Geomechanical response of permafrost-associated hydrate deposits to depressurization-induced gas production. J. Petrol. Sci. Eng. 2009, 67(1-2): 1-12.

Schoderbek, D., Farrell, H., Hester, K., et al. ConocoPhillips gas hydrate production test final technical report, October 1, 2008-June 30, 2013. DOE Award No.: DE-NT0006553 Search PubMed, 2013.

Selim, M., Sloan, E. Heat and mass transfer during the dissociation of hydrates in porous media. AIChE J. 1989, 35(6): 1049-1052.

Shen, J., Chiu, C.F., Ng, C.W.W., et al. A state-dependent critical state model for methane hydrate-bearing sand. Comput. Geotech. 2016, 75: 1-11.

Sloan, E.D., Koh, C. Clathrate hydrates of natural gases. Florida, USA: CRC press, 2007.

Song, Y., Zhu, Y., Liu, W., et al. Experimental research on the mechanical properties of methane hydrate-bearing sediments during hydrate dissociation. Mar. Petrol. Geol. 2014, 51(0): 70-78.

Sun, X., Guo, X., Shao, L., et al. A thermodynamics-based critical state constitutive model for methane hydrate bearing sediment. J. Nat. Gas. Sci. Eng. 2015, 27: 1024-1034.

Sun, X., Nanchary, N., Mohanty, K.K. 1-D modeling of hydrate depressurization in porous media. Transport Porous Med. 2005, 58(3): 315-338.

Uchida, S., Xie, X.G., Leung, Y.F. Role of critical state framework in understanding geomechanical behavior of methane hydrate-bearing sediments. J. Geophys. Res-Sol. Ea. 2016, 121(8): 5580-5595.

Vedachalam, N., Srinivasalu, S., Rajendran, G., et al. Review of unconventional hydrocarbon resources in major energy consuming countries and efforts in realizing natural gas hydrates as a future source of energy. J. Nat. Gas. Sci. Eng. 2015, 26: 163-175.

Wang, Y., Li, X.S., Li, G., et al. Experimental study on the hydrate dissociation in porous media by five-spot thermal huff and puff method. Fuel 2014, 117, Part A(0): 688-696.

Yamamoto, K., Terao, Y., Fujii, T., et al. Operational overview of the first offshore production test of methane hydrates in the Eastern nankai Trough. Paper OTC25243 Presented at Offshore Technology Conference, Houston, Texas. 05-08 May. 2014.

Yoneda, J., Masui, A., Konno, Y., et al. Mechanical properties of hydrate-bearing turbidite reservoir in the first gas production test site of the Eastern Nankai Trough. Mar. Petrol. Geol. 2015, 66: 471-486.

Yun, T.S., Santamarina, J.C., Ruppel, C. Mechanical properties of sand, silt, and clay containing tetrahydrofuran hydrate. J. Geophys. Res. 2007, 112(B4): B04106.

Zhang, X.H., Lu, X.B., Zhang, L.M., et al. Experimental study on mechanical properties of methane-hydrate-bearing sediments. Acta. Mech. Sinica-Prc. 2012, 28(5): 1356-1366.

Zhang, X.H., Lu, X.B., Shi, Y.H.,et al. Study on the mechanical properties of hydrate-bearing silty clay. Mar. Petrol. Geol. 2015, 67: 72-80.

Zhang, X.H., Luo, D.S., Lu, X.B., et al. Mechanical properties of gas hydrate-bearing sediments during hydrate dissociation. Acta. Mech. Sinica-Prc. 2017: 1-9.